Journal of Fluids Engineering. February 19, 2025;
Accepted manuscript posted May 23, 2025. 10.1115/1.4068762

Yutaka Kaneko
Institute of Fluid Science,
Tohoku University,
2-2-1, Katahira, Aoba-ku,
Sendai-shi, Miyagi, Japan;
email: y-kaneko@tohoku.ac.jp

Shūji Ōtomo
Department of Mechanical Systems Engineering,
Tokyo University of Agriculture and Technology,
2-24-16, Naka-cho,
Koganei-shi, Tokyo, Japan
email: otomo@go.tuat.ac.jp

Taisuke Torin
Department of Mechanical Systems Engineering,
Tokyo University of Agriculture and Technology,
2-24-16, Naka-cho,
Koganei-shi, Tokyo, Japan

Yusuke Kakuya
Department of Mechanical Systems Engineering,
Tokyo University of Agriculture and Technology,
2-24-16, Naka-cho,
Koganei-shi, Tokyo, Japan

Takafumi Saito
Department of Mechanical Systems Engineering,
Tokyo University of Agriculture and Technology,
2-24-16, Naka-cho,
Koganei-shi, Tokyo, Japan

Tatsuhiko Hanai
Department of Mechanical Systems Engineering,
Tokyo University of Agriculture and Technology,
2-24-16, Naka-cho,
Koganei-shi, Tokyo, Japan

Takashi Matsuno
Department of Mechanical and Physical Engineering,
Tottori University,
4-101, Koyama-cho Minami,
Tottori-shi, Tottori, Japan
email: matsuno@tottori-u.ac.jp

Hiroyuki Nishida[1]
Department of Mechanical Systems Engineering,
Tokyo University of Agriculture and Technology,
2-24-16, Naka-cho,
email: hnishida@cc.tuat.ac.jp

Accepted manuscript:
Version of Record: Y. Kaneko, S. Ōtomo, T. Torin, Y. Kakuya, T. Saito, T. Hanai, T. Matsuno, and H. Nishida, “The Combination of Rear Flaps and Plasma Actuators for the Drag Reduction of a Square-Back Bluff Body,” Journal of Fluids Engineering, Vol. 147, No. 12, 121201 (2025).
DOI: 10.1115/1.4068762
The published Version of Record is available from the ASME Digital Collection: https://doi.org/10.1115/1.4068762

The Combination of Rear Flaps and Plasma Actuators for the Drag Reduction of a Square-Back Bluff Body

There is a significant need to reduce the aerodynamic drag of ground vehicles. As a result, the active and passive methods of flow control around bluff bodies have been extensively studied to improve aerodynamic performance. In this study, the drag reduction by combining rear flaps and plasma actuators (PAs) is experimentally investigated. PAs are modern active flow control devices that leverage non-thermal plasma, whereas flaps are traditional passive flow control devices. Flaps and PAs are mounted on the square back of the truck model, and the effect of the flap mounting locations (top or side of the model), flap angle, and flap length are investigated at $Re_H = 1.58 \times 10^5$*. For both top and side flaps, the longer flaps result in greater drag reduction compared to shorter flaps in the absence of PA actuation. However, additional drag reduction with PA actuation is minimal for the longer flaps, and the flap angle at which drag reaches a local minimum remained unchanged. This is attributed to an increase in pressure drag on the flap as the flap angle increases when the flow is attached to the flap surface. In contrast, PA actuation with shorter flaps demonstrates drag reduction, due to the smaller surface area of the flaps. These results suggest that optimising the flap angle and length is a promising strategy to maximise the aerodynamic benefits of PA actuation and reduce the drag on bluff bodies.*

Keywords: square-back bluff body, drag reduction, rear flap, plasma actuator

Journal of Fluids Engineering. February 19, 2025;
Accepted manuscript posted May 23, 2025. 10.1115/1.4068762

1 Introduction

The CO_2 consumption in transportation is a worldwide problem. There is an urgent need for reducing the CO_2 emission from ground transportation by road vehicles since it occupies a third-quarter of the total emission in transportation [1]. According to previous studies [e.g. 2,3], the aerodynamic drag of ground vehicles is more than 50% of the total energy consumption on a highway. Therefore, it is necessary to reduce the aerodynamic drag of ground vehicles to improve energy efficiency. To this end, there have been many studies in bluff body aerodynamics to well understand complex three dimensionality and unsteadiness of flowfield, massive separation at the rear edge, a large wake of rear vehicle, and so on [4].

In the previous studies, some well-known simplified models, Ahmed [5], GM [6], and Windsor [7] models, have been used to gain insight into the complex flowfield around the bluff body. Ahmed model [8] has a slanted rear surface to represent a fast-back vehicles. On the other hand, GM model [6] which was proposed by General Motors has a square-back shape. They are well summarized in the review article by Choi et al. [4]. Windsor model [9], which has a more realistic front geometry with a square-back shape, has been also adopted in several studies on bluff body aerodynamics.

Zhang et al. [10] conducted extensive hot-wire, flow visualization, and particle image velocimetry (PIV) at $Re = \mathcal{O}(10^5)$ and clarified the unsteady predominant coherent structures formed around an Ahmed body. They presented a conceptual model illustrating the flow structures around the Ahmed model, based on various flow field measurements from the literature and previous studies. Their model incorporates predominant unsteady flow structures formed above the roof, over the side surface and the rear window, and behind the base of the Ahmed model along with their corresponding dimensionless frequencies. This provides insights into flow control strategies. There are some studies addressing the effect of curvatures of a bluff body [11,12], and it has been shown that they are also important factors in achieving better aerodynamic performance. Thacker et al. [13] investigated the effect of edge shape (sharp or round edge) at roof and rear slant of an Ahmed body on flow topology and aerodynamic force at $Re \approx \mathcal{O}(10^6)$. They showed that the round edge connection prevent the separation bubble on the rear slant, and it contributed to the drag reduction of 10%. Also, Rossitto et al. [14] conducted a systematic investigation focusing on the effects of rounding of an upper edge and side pillars of an Ahmed body at $Re = \mathcal{O}(10^6)$. Although the flowfield was strongly and locally modified due to the additional rounding of side pillars, there was no drag modification because of the zero net drag effects on the slanted and vertical surfaces. In reality, wheels seems to affect the underbody flow and resultant drag on a bluff body. Therefore, some literature added wheels to the simplified models, and the effect of the wheels has been also investigated. Bao et al. [15,16] placed D-shaped obstacles in the underflow of a Windsor body to mimic wheels and examined wheel-vehicle aerodynamic interaction through numerical and experimental analysis ($Re = \mathcal{O}(10^5)$). They showed that the distance between the obstacles and the base of the body had effect on the wake topology. Pavia et al. [17] visualized the unsteady wake of an Windsor body with wheels at $Re = \mathcal{O}(10^5)$ using large-scale tomographic PIV. Due to the addition of wheels, the vertical symmetry of wake vanished and an upwash-dominated wake was formed. There have been other studies considering real environment such as yaw effect [18,19], ground effect [20,21], and so on.

Drag can be divided into friction and pressure drags. As the major part of the drag of the bluff body is pressure drag due to flow separation (so-called form drag) [5,22], researchers have been tackling to control the flow separation around the body both in passive and active manners.

For passive flow control, several techniques such as fairing [23], flap [24,25], and vortex generator [26] are effective in reducing drag. Giannenas et al. [27] conducted a two-dimensional simulation of the flowfield around a square-cylinder wake at a Reynolds number of $Re = 100$. They showed that periodically pitching flaps decreased drag up to 12.0%. Garcia et al. [28] located two flaps on the rear lateral edges of an Ahmed body and investigated the effect of two flap angles which were varied individually at various yaw angles. Their parametric study clarified that the asymmetrical flaps can obtain minimum drag and there are optimal asymmetrical flap settings for each yaw angle. Beaudoin and Aider [24] used an Ahmed body and investigated the effect of the location of the rear flaps and

[1]Corresponding Author.
Version 1.18, May 13, 2025

its angle on drag. They achieved 25.5% drag reduction with a combination of multiple flaps which were mounted on all rear edges at an optimal angle. Recently, the effectiveness of adaptive flaps has been confirmed in flow control around an Ahmed body [29]. Muñoz-Hervás et al. [30] used flexible rear flaps on the side edge of an Ahmed body and investigated the effect of flaps deflecting in response to the flowfield at $Re = \mathcal{O}(10^4)$. Their experiments revealed that the flexible flaps could effectively reduce the drag on an Ahmed body even if it was under cross-flow conditions, and achieved 8.4% drag reduction under aligned conditions.

On the other hand, active flow control, such as blowing [31,32] and suction [33] has been also applied to reduce drag on bluff bodies. Plasma actuators (PAs) that energize dielectric-barrier-discharge have also got much attention and expected as alternative active flow control devices [34–36]. A typical PA consists of a dielectric layer and two electrodes that are asymmetrically installed on both sides of the dielectric layer [37,38]. One electrode is exposed to the air and the other is encapsulated with insulating material. No moving parts and switching on and off by electrical signal enable PAs to control flow in a very fast response. In addition, thanks to its thin structure, PAs can be installed easily on various body surfaces [39]. There have been many studies on the application of PAs for flow control around various bodies, such as airfoils [40,41] and cylinders [42,43]. The power flow diagram of PAs from an electrical input power to aerodynamical effects is illustarated in Fig. 1, which was also discussed in detail by Rodrigues et al. [44]. When a high voltage (typical several kVpp), exceeding the breakdown voltage of air, is applied to the electrodes, the accelerated electrons cause the generation of non-thermal plasma, which consists of electrons, charged particles, excited atoms and molecules, and neutral particles. When PAs are driven by an AC high-voltage, a part of electrical power is dissipated as dielectric heating. The charged particles in the plasma are accelerated by the electric field and then transports momentum to the ambient air in a collision, resulting in the wall-surface jet in quiescent air [45–47]. This fluid mechanical power enables PAs to control the flow, leading to various aerodynamic benefits such as drag reduction, turbulent drag reduction [48], lift enhancement, noise reduction [49], and so on. Meanwhile, plasma maintenance power is also dissipated as heat loss (Joule heating), caused by electronically excitation collisions, rotational and vibrational excitation, ion-netural molecule collisions [50–52]. Previous studies demonstrated various applications of PA utilizing this thermal energy, including anti- and de-icing above airfoils [53], and flow separation control with nanosecond high-voltage application [54].

Some researchers have reported the application of PA to bluff bodies or truck models. Kim et al. [55] installed a PA on a slant edge of an Ahmed body and investigated the effect of the spanwise length of PA and applied voltage. They achieved the 10% reduction of drag at a freestream velocity of $u_\infty = 10$ m s^{-1} ($Re = \mathcal{O}(10^5)$) and clarified that the PA actuation could suppress flow separation above the slanted surface through flowfield visualization and pressure measurement. Rodrigues et al. [56] performed experiments for three different slant angles, 30, 40, and 60°, of an Ahmed body and succeeded in delaying flow separation and narrowing the wake for the slant angle of 60° at $u_\infty = 5$ m s^{-1} ($Re \approx \mathcal{O}(10^5)$). Vernet et al. [57] and Roy et al. [58] applied PAs to practical vehicle models which had more complicated shapes and investigated the flow control effect by PA actuation.

Although there have been many studies on either passive or active flow controls on bluff bodies as reviewed above, the combination of both techniques seems scarce. El-Alti et al. [59] used synthetic jets along with flaps for a full-scale truck model. They showed that the combination of passive and active flow control devices led to a 4.3 - 5.4% reduction in fuel consumption compared with the case using only flaps. It suggests that the combination of two or more types of flow control devices can lead to a drastic reduction in drag and hence fuel consumption.

This study aims to clarify the drag reduction of the square-back bluff body by the combination of rear flaps and PAs through direct force measurement and particle image velocimetry (PIV). Optimal length and angle of the rear flaps are sought. In addition, we conduct two types of experiments which vary the side of mounting flaps; top and side of vehicle.

The rest of the paper is organized as follows. Section 2 describes a truck model used in this study and methodologies of force measurement and PIV. Section 3 discusses the optimal length and angle of the rear flap mounted on top of the model for aerodynamic performance improvement by PA actuation. Similarly, the effects of length and angle of side flaps on aerodynamic performance improvement by PA actuation are clarified. Then, a comparison is made between the effects of top and side flaps on aerodynamic performance improvement by PA actuation. Finally, the conclusions are drawn in Sect. 4.

Journal of Fluids Engineering. February 19, 2025;
Accepted manuscript posted May 23, 2025. 10.1115/1.4068762

2 Experimental method

2.1 Truck model. Figure 2(*a*) shows the square-back bluff body model used in the experiments. While most of previous studies in vehicle aerodynamics employ either Ahmed or Windsor bodies as reviewed in the previous section, we design the bluff body model having the streamlined nose on both top and sides as shown in Fig. 2(*a*). This is because we focus on the aerodynamic effect of top and side rear flaps combined with PAs, which requires the flow attached on the carriage walls. As shown in Fig. 2(*b*), therefore, the fairing (black) was mounted on the front of the truck model (purple and gray). The gap between the fairing and the model is sealed with tape. The truck model is manufactured by Tokyo Fluid Research Co., Ltd. using a stereolithography apparatus. The fairing is homemade by 3D printing. The wheels are represented by rigid semicircular cylinders and fixed to the model body, resulting in no rotation during experiments. The height H, width W and length L of the model is 0.250 m, 0.190 m, and 0.732 m, respectively. Since the width of the wheels of the model is 0.040 m, the cross-sectional area A of the model is calculated as $A = 4.99 \times 10^{-2}$ m^2.

Rear flaps are made by bending a part of acrylic plates smoothly at angle α as shown in Fig. 3(*a*). As mentioned below, the acrylic plates are also used as a dielectric plate of PA. The acrylic plates are flush-mounted on the top or sides of the model, and bent sections are used as rear flaps. Figure 4 shows the examples of rear flaps on the (a) top and (b) sides. As can be seen from Fig. 4, the top or side walls, which are not equipped with PA-mounted flaps, are extended to have the same length as the flaps. It enables us to see the effect of one side flap on the aerodynamic performance. For example, when the flap is mounted on the top of the model (Fig. 4(*a*)), two acrylic plates are mounted on the side. Table 1 summarizes the conditions of flaps. We test two different flap lengths, l = 10 mm and 50 mm, and flap angles α are varied from 0° to 30°. Note that the overall length of the model becomes $L + l\cos\alpha$. This makes the overall length 0.782 m at α = 0° and 0.775 m at α = 30° for l = 50 mm, and thereby the difference is negligible. The flap lengths shown in the table are non-dimensionalized by the height of the truck model H.

Acrylic rear flaps with 2 mm thickness are used as a dielectric plate as shown in Fig. 3(*b*). Copper tapes of 0.07 mm thickness are placed on both sides of the acrylic plate asymmetrically with 0 mm overlap between the electrodes. The spanwise length of the electrodes is 0.150 m, which is about 79% of the width of the truck model W = 0.190 m. The exposed electrode is serrated to generate plasma uniformly along the spanwise direction. Both the height of the tips and the distance between two successive tips are 1 mm. The PA is set so that the serration tips of an exposed electrode are on the bending point of the rear flap. We use a high-voltage amplifier (PSI, PSI-series) to drive the PA. The frequency and applied voltage are 5 kHz and 20 kV$_{\mathrm{pp}}$, respectively. The voltage applied to the PA is monitored using the high-voltage probe (Tektronix, P6015A) and the oscilloscope (Tektronix, TDS2024B).

2.2 Force measurement. The experiments are performed in the suction-type low-speed wind tunnel at Tottori University. As shown in Fig. 5, the truck model is placed in the test section of 0.6 m width and height. It results in a blockage ratio of approximately 14%. Although this blockage ratio is relatively high, the blockage correction is not applied in this research because we focus on the drag reduction due to the combination of PAs and rear flaps rather than the absolute values. Four wheels of the model are mounted on a stage, which is rigidly connected to a 6-component load cell (Nissho Electric Works, LMC-61187) such that they do not touch the wind tunnel floor and flow disturbance is as minimal as possible. The freestream velocity u_∞ is fixed at 10 m s^{-1} by monitoring a pitot tube in the test section and a differential pressure gauge (Halstrup Walcher, KAL84). The Reynolds number based on the model height H is $Re = u_\infty H/\nu = 1.58 \times 10^5$, and the turbulent intensity is 0.7%.

The signal of the aerodynamic balance is sent to a signal conditioner and acquired by a data acquisition board (DAQ) (National Instruments). To minimize the electromagnetic noise due to PA activation, several ferrite cores are attached to the cables covered by electromagnetic shields. In addition, the raw signals are low-pass filtered by a signal conditioner with the cut-off frequency f_c of 100 Hz. The cut-off frequency is chosen based on the estimation of dominant frequency f_d associated with flow structures around the body. According to previous study [10], the Strouhal numbers of the unsteady flow structures targeted for control using flaps and PAs in this study - namely, the side vortex (St_s) and the flow structures emanated from the upper and lower bubbles (St_w) - range from 0.25 to 0.54. Therefore, the frequency associated with these flow structures can be estimated as $f_d < St u_\infty/H$ = 21.6 Hz, resulting in the cut-off frequency of 100 Hz which is sufficiently higher than this frequency. The force measurement is conducted for $t = 10$ s ($tu_\infty/L = 140$) at a sampling rate of 1000 Hz. As a result, the time-series data of 10000 points are obtained, following which the signals are averaged. Figure 6 shows the results of averaging-time (sampling duration) convergence. The plotted data originate from the time-series data obtained under the same condition: $l^* = 0.04$, $\alpha = 10°$, with the PA actuation. The measured voltage converges as the averaging time increases, indicating that a sampling duration of 10 seconds is sufficient. For each condition, more than four trials are performed to verify repeatability. The time-averaged drag force and its standard deviation are then calculated from these measurement results. As preliminary experiments, the force measurements without operating the wind tunnel are conducted with and without driving the PA. The difference is subtracted from the results obtained with the actuation of PA in freestream to remove the effect of magnetic noise. From the time-averaged drag D, we calculate drag coefficients C_D and drag reduction rate DR as,

$$C_D = \frac{D}{\frac{1}{2}\rho u_\infty^2 A}, \quad (1)$$

and

$$DR = \frac{C_{D,\text{off}} - C_{D,\text{on}}}{C_{D,\text{off}}}, \quad (2)$$

where the subscript 'on' and 'off' means that PA is driven or not, respectively.

2.3 Particle image velocimetry. Particle image velocimetry (PIV) is conducted for two different cross-sections depending on the flap types as shown in Fig. 7. In the cases where a flap is mounted on top, a laser is irradiated from above the test section so that the laser sheet is perpendicular to the wind tunnel floor (Fig. 7(*a*)). A measurement cross-section is at the centre of the model and images are recorded by a high-speed camera (Photron, Fastcam Mini, 1024 × 736 pixels) equipped with a zoom lens (Nikon, AF-S Nikkor 24-120 mm f/4G ED VR). As can be seen in Fig. 7(*b*), in the cases where flaps are mounted on the two sides of the model, the positions of the laser and camera are swapped. The laser is irradiated parallel to the floor at a height of 0.208 m ($z/H = 0.83$). In this study, two types of laser systems, a continuous wave laser (Dantec Dynamics, RayPower2000) with a cylindrical lens (Seika, BZ-61N) or a double pulse laser (Lee laser, EN60825-1), are used. Note that we confirm that there is not a significant difference between the particle images obtained using different laser systems. For tracer particles, two fog machines (ANTARI, Z-1500 and Z-800) are placed upstream of the suction nozzle of the wind tunnel. The fog liquids (ANTARI, FLG 6; water 48-51%, propylene glycol 30-32%, glycerin 19-20%) are used. Estimating the diameter d and the particle density ρ_p of tracer particles at 10 μm and 1.9 kg/m^3, respectively, the Stokes number Sk is calculated as $Sk = \rho_p d^2 u_\infty/18\mu H = 2.3 \times 10^{-5} \ll 1$. Therefore, the tracer particles highly follow the turbulent flow. 10000 instantaneous images are acquired at the frame rate of 3000 fps, exposure time of 1/3000 s, and resolution of approximately 0.3 mm/pixel. As a result, we obtain 5000 instantaneous snapshots by image-correlation. The velocity vectors are calculated using Koncert II software (Seika). The multi-grid interrogation with final window sizes of 24 pixels is used. The overlap of interrogation windows is 50%, resulting in a physical resolution of 7.2 mm ($2.88 \times 10^{-2}H$) with the grid spacing of 3.6 mm ($1.44 \times 10^{-2}H$). The outliers are eliminated using the universal outlier detection [60] and then interpolated.

3 Results and discussions

3.1 Top rear flaps. Here we show the results of the top rear flap and discuss its flow control effect. Figures 8(*a*) and 8(*b*) respectively show the drag coefficient C_D and drag reduction rate DR as a function of top flap angle α. The open and closed markers represent the results obtained without (w/o) and with (w/) PA actuation, respectively. For both flap lengths, drag force decreases with increasing flap angle α, and increases after reaching the local minimum. This evolution of drag force in relative to change in flap angle is qualitatively in line with that of previous studies [24,61]. However, a sharp increase (or decrease) of drag around the critical angle, the so-called 'drag crisis' is not observed in this study. When the PA is not driven, the longer flap ($l^* = 0.20$, diamond markers) can decrease C_D

more than the shorter flap ($l^* = 0.04$, square markers). For DR, Fig. 8(b), we find that the shorter flaps have the advantage over the longer flaps when the PA is actuated. In the following, we discuss the results in detail.

We focus on and discuss the results of longer flaps ($l^* = 0.20$). C_D without PA actuation takes local minimum value between $\alpha = 10°$ and 15° and rapidly increases at $\alpha = 25°$. From Fig. 8(b), DR below $\alpha = 20°$ is around 0% indicating that C_D is not decreased by PA actuation below $\alpha = 20°$. At higher flap angles ($\alpha = 25°$ and 30°), C_D is decreased by PA actuation shown in Fig. 8(a), also shown as increases in DR up to 2% without error bars overlapping 0% line (Fig. 8(b)). However, C_D at $\alpha = 25°$ and 30° is still higher than that at $\alpha = 10°$ without PA actuation (blue diamond, $C_D = 0.589$). Figures 9(a), 9(b), and 9(c) show the time-averaged flowfields without PA actuation respectively at $\alpha = 0°$, 15°, and 25°. White rectangles on the left-hand side represent the model and flap, and $x/H = 0$ and $z/H = 0$ correspond to the back of the model and the ground of the wind tunnel, respectively. Gray arrows show the velocity vectors. The dashed lines in the figure represent the 15° line along the flap of $\alpha = 15°$. We can see that the wake region of the model is dominated by the flow from the bottom of the model, and a large counterclockwise recirculating flow is formed behind the model. As indicated in many previous studies, the time-averaged wake represents the symmetrical flowfields in both vertical and lateral directions when there is no wheel. As indicated in many previous studies, the time-averaged wake in a two-dimensional cross-section represents a line-symmetrical flowfield in both vertical and lateral directions when there is no wheel. On the other hand, as described by Pavia et al. [17], the wheels caused the loss of vertical symmetry of wake and the formation of upwash-dominated wake. Since the model used here has wheels, the flowfields represent the asymmetry and upwash-dominated wake. Flow along the top of the model is not deflected when there is no flap angle (Fig. 9(a)). As shown in Fig. 9(b), the flow is attached to the flap and the wake region becomes narrower at $\alpha = 15°$, leading to the reduction of C_D. Increasing α to 25° (Fig. 9(c)), the fluid cannot flow along the top flap and separated from the flap. As a result, the wake region becomes wider than that of $\alpha = 15°$. In response to this change in the wake region, drag increases.

Figure 9(d) shows the flowfield at $\alpha = 25°$ with PA actuation. Comparison of Figs. 9(c) and 9(d) reveals that the separated flow is successfully attached by the PA actuation, and the wake region remarkably gets narrower. The modification of the wake region by PA leads to more than 3% drag reduction as shown in Fig. 8(b). In addition, comparing Figs. 9(d) with 9(b), the wake region at $\alpha = 25°$ with PA actuation is narrower than that at $\alpha = 15°$ without PA actuation. However, as shown in Fig. 8(a), C_D at $\alpha = 25°$ with PA actuation (red triangle) is not below that at $\alpha = 15°$ without PA actuation (blue diamond). This is due to the pressure drag on the flap itself. There is a pressure difference between both surfaces of the flap, which causes the normal force on the flap itself. As the flap angle increases, the normal force and its streamwise component, drag, becomes larger. This is why C_D is not decreased even though the wake region gets narrower by increasing the flap angle. Therefore, decreasing the flap area should be effective to decrease the drag on flap (i.e., drag force on the model) for larger α.

Here we discuss the results of the shorter flap length ($l^* = 0.04$). As can been seen from Fig. 8(a), C_D of the short flap without PA actuation also takes local minimum value at $\alpha = 10°$. Figure 8(b) represents that DR is more than 0 for $\alpha \geq 10°$. It means that PA actuation is effective when it is used with a short flap. In addition, PA actuation increases the critical α where C_D takes the local minimum value from 10° to 20°. Therefore, the smaller surface of flaps enables the PA to reduce C_D even at a larger flap angle. Figure 10 shows the flowfields when a short flap is installed. In Figs. 10(b) and 10(c), the 20° lines are also drawn. From the comparison between Figs. 10(a) $\alpha = 0°$ and 10(b) $\alpha = 20°$ without PA actuation, we can find the short flap at $\alpha = 20°$ can not deflect the flow above the model along the flap. In fact, in this case, the drag does not change. We can also find that the PA actuation modifies the wake region only slightly from Figs. 10(b) and 10(c). Nevertheless, due to the PA actuation, C_D decreases, and DR reaches approximately 3% as shown in Fig. 8(b).

Here, we make a comparison between the results of long and short flaps. Comparing Fig. 9(d) with Fig. 10(c), the wake region of the short flap is wider. However, C_D of the short rear flap is smaller. As mentioned above, this is because the normal force acting on the flap contributes to drag. Since the long flap has a wider surface, the normal force acting on the long flap is larger when the flow is attached to the flap surface. From the above results and discussions, we can make the following conclusions. Without PA actuation, C_D

can be reduced more effectively using longer flaps than shorter ones. There is an optimal length of the flap where the drag reduction is effective by using the PA along with the flap.

3.2 Side rear flaps. Figures 11(*a*) and 11(*b*) respectively plots drag coefficient C_D and DR as a function of side flap angle α. Circles and triangles respectively represent the results of longer ($l^* = 0.20$) and shorter side flaps ($l^* = 0.04$). The drag is smaller than that shown in the above subsection (Fig. 8(*a*)). Side rear flaps are mounted on two sides of the vehicle model, while the top flap is mounted on only the top side of the model. Therefore, there is a difference in the wake flow and resultant drag between the rear flap conditions. Longer side flaps drastically decrease C_D, and minimum $C_D = 0.551$ in this paper is achieved at $\alpha = 15°$. However, as can been seen from Fig. 11(*b*), PA actuation has little effect on C_D in this condition. A general trend that C_D takes the local minimum value at the specific flap angle α is the same as that of the top flap. When the longer flaps are mounted, the α where C_D takes the local minimum value is 15° whether or not PAs are actuated. On the other hand, PA actuation with short side flaps increases the α of the local minimum from 10° to 15° or 20°. Similarly to the top flap cases, C_D reduction by PA actuation is observed when PA is used with shorter flaps.

Figure 12(*a*) shows the flowfields for longer flaps at $\alpha = 0°$, measured at $z/H = 0.83$. We can see that there is a large reverse flow behind the model. As previously shown in Figs. 9 and 10, the wake formed behind the model is counterclockwise recirculating flow, and the flow at $z/H = 0.83$ directs toward the back of the model. Therefore, the reverse flow shown in Fig. 12 is not from the side of the model, but the upwash flow. Figure 12(*b*) shows the flowfields at $\alpha = 15°$. The upper and lower of the figure represent that without and with PA actuation, respectively. As well as the figures in the above subsection, 15° lines along the flaps are also depicted. Comparing Fig. 12(*a*) and upper of Fig. 12(*b*), side flaps dramatically modify the wake structure, resulting in the minimum C_D as shown in Fig. 11(*a*). In addition, the long flap at $\alpha = 15°$ can attach the flow without PA actuation. Therefore, the comparison of upper and lower figures of Fig. 12(*b*) shows little difference in the flowfield. It is the reason why C_D does not change by the PA actuation when the long flaps are mounted on side at $\alpha = 15°$. Figure 13 compares the flowfields when the short flaps are mounted on sides at α of (a) 0°, (b) 15°, and (c) 30°. As with the long flaps, the shorter flap also deflects side flows and makes the narrower wake region as compared in Figs. 13(*a*) and 13(*b*). Note that the effect of short flaps on the wake is less than that of long flaps. Increasing flap angle α, Fig. 13(*c*), the deflection effect by flaps becomes smaller due to separation. At both Figs. 13(*b*) $\alpha = 15°$ and 13(*c*) $\alpha = 30°$, PA actuation affects the flowfield and makes the wake region narrower. However, the side flows do not follow the 15° lines when the PAs are actuated above the short flaps (Figs. 13(*b*) and 13(*c*)), whereas the long flaps guide the side flows along the 15° lines almost perfectly as shown in Fig. 12(*b*). Therefore, the wake region formed by PA actuation above the short flaps is wider than that formed when long flaps are mounted at $\alpha = 15°$, resulting in a larger C_D than that of long flaps. To achieve the fully attached flow and more decrease in C_D by using PA and short flaps, burst actuation may be one of the options [62–65].

4 Conclusions

In this paper, we have experimentally clarified the drag reduction of the square-back bluff body by the combination of the rear flaps and PAs. The truck model with wheels has been used, and the force measurements and flow visualizations at $Re_H = 1.58 \times 10^5$ have been conducted varying the side of mounting flaps; top and side of the vehicle. In addition, the effects of the flap length and angle have been also investigated. The longer flap mounted on the top of the vehicle modified the wake region and decreased C_D. In addition, C_D changed depending on the flap angle and had a local minimum value. However, there was little effect of PA actuation with a longer flap on C_D, i.e., there is no additional drag reduction. Although the flow behind the model could be modified with the PA actuation, the flap angle where the C_D took a local minimum did not change. This was because the attaching flow to the flaps by PA actuation increased the pressure drag. Therefore, the PA actuation with the shorter flaps decreased the C_D because of its smaller surface area of flaps and pressure drag on the flaps. The above results suggested that the flap length (surface area) have to be optimized to realize a further drag reduction by the PA actuation. As well as the top flap, the PAs reduced C_D when it was actuated above the shorter flap. A comparison

Journal of Fluids Engineering. February 19, 2025;
Accepted manuscript posted May 23, 2025. 10.1115/1.4068762

of the results of the top and side flaps revealed that the side flaps decreased C_D more than the top flap because of a larger number of flaps and drastic modification of the wake region.

This study indicates the optimization of the length, angle and mounting surface of the flap is the key factor in achieving extensive drag reduction by the combination of flap and PAs, based on force measurement and PIV results. Although the two-dimensional flow visualizations conducted in this study successfully explain the changes in aerodynamic performance due to the flaps and PA actuation, the wake of the model must be three-dimensional. For a full understanding of the aerodynamic effects of flaps and PA actuation, flow visualizations in multiple planes or three-dimensional PIV are required. This is the subject of further studies. Furthermore, the effect of the driving mode of PAs such as continuous or burst actuation has not been investigated. As mentioned in the results section, the burst actuation of PAs has been shown to work effectively for separation flow control of airfoils in many studies. Therefore, the optimization of the flap conditions along with the conditions of PA actuation has the potential to achieve further drag reduction of square-back bluff bodies. This will be tackled in future work.

Acknowledgment

This research is financially supported by Mitsubishi Fuso Truck and Bus Corporation (Mr. Yoshihiro Inoue (Manager), Mr. Kenji Yaguchi (Assistant Manager), and Mr. Hiroshi Ohkunitani (Assistant Manager)). We also greatly appreciate Mr. Shoichi Matsumoto, Mr. Yukihiro Takahashi, Mr. Taketo Sato, Mr. Kengo Tomokawa, and Mr. Takumi Nankaku for their sincere support in performing experiments.

Nomenclature

A = cross-sectional area (m^2)
C_D = drag coefficient, $2D/\rho u_\infty^2 A$
D = drag (N)
d = diameter of tracer particles (m)
DR = drag reduction rate (%)
f_c = cut-off frequency (Hz)
f_d = dominant frequency (Hz)
H = truck height (m)
L = truck length (m)
l = flap length (m)
l^* = non-dimensional flap length, l/H
Re = Reynolds number, $u_\infty H/\nu$
Sk = Stokes number, $\rho_p d^2 u_\infty/18\mu H$
St = Strouhal number, fH/u_∞
$\boldsymbol{u}$ = velocity vector (m s^{-1})
u_∞ = free stream velocity (m s^{-1})
$|\boldsymbol{u}|$ = velocity magnitude (m s^{-1})
W = truck width (m)
α = flap angle (°)
μ = viscosity (Pa s)
ν = dynamic viscosity (m^2 s^{-1})
ρ = fluid density (kg m^{-3})
ρ_p = particle density of tracer particles (m^{-3})

References

[1] Ritchie, H., 2020, "Cars, planes, trains: where do CO_2 emissions from transport come from?" Our World in Data.

[2] Hucho, W. and Sovran, G., 1993, "Aerodynamics of Road Vehicles," Annual Review of Fluid Mechanics, **25**, pp. 485–537.

[3] Barros, D., Borée, J., Noack, B. R., Spohn, A., and Ruiz, T., 2016, "Bluff body drag manipulation using pulsed jets and Coanda effect," Journal of Fluid Mechanics, **805**, pp. 422–459.

[4] Choi, H., Lee, J., and Park, H., 2014, "Aerodynamics of heavy vehicles," Annual Review of Fluid Mechanics, **46**, pp. 441–468.

[5] Ahmed, S., Ramm, G., and Faltin, G., 1984, "Some salient features of the time-averaged ground vehicle wake," SAE Technical Paper, p. 840300.

[6] Han, T., Sumantran, V., Harris, C., Kuzmanov, T., Huebler, M., and Zak, T., 1996, "Flow-Field Simulations of Three Simplified Vehicle Shapes and Comparisons with Experimental Measurements," *International Congress and Exposition*, SAE International, doi: 10.4271/960678.

[7] Haffner, Y., Li, R., Meldi, M., and Borée, J., 2022, "Drag reduction of a square-back bluff body under constant cross-wind conditions using asymmetric shear layer forcing," International Journal of Heat and Fluid Flow, **96**, p. 109003.

[8] Aleyasin, S. S., Tachie, M. F., and Balachandar, R., 2021, "Characteristics of flow past elongated bluff bodies with underbody gaps due to varying inflow turbulence," Physics of Fluids, **33**(12), p. 125106.

[9] Islam, A., Gaylard, A., and Thornber, B., 2017, "A detailed statistical study of unsteady wake dynamics from automotive bluff bodies," Journal of Wind Engineering and Industrial Aerodynamics, **171**, pp. 161–177.

[10] Zhang, B. F., Zhou, Y., and To, S., 2015, "Unsteady flow structures around a high-drag Ahmed body," Journal of Fluid Mechanics, **777**, p. 291–326.

[11] Fuller, J. and Passmore, M. A., 2014, "The importance of rear pillar geometry on fastback wake structures," Journal of Wind Engineering and Industrial Aerodynamics, **125**, pp. 111–120.

[12] Perry, A.-K., Pavia, G., and Passmore, M., 2016, "Influence of short rear end tapers on the wake of a simplified square-back vehicle: wake topology and rear drag," Experiments in Fluids, **57**, p. 169.

[13] Thacker, A., Aubrun, S., Leroy, A., and Devinant, P., 2012, "Effects of suppressing the 3D separation on the rear slant on the flow structures around an Ahmed body," Journal of Wind Engineering and Industrial Aerodynamics, **107-108**, pp. 237–243.

[14] Rossitto, G., Sicot, C., Ferrand, V., Borée, J., and Harambat, F., 2016, "Influence of afterbody rounding on the pressure distribution over a fastback vehicle," Experiments in Fluids, **57**, p. 43.

[15] Bao, D., Borée, J., Haffner, Y., and Sicot, C., 2022, "Near wake interactions and drag increase regimes for a square-back bluff body," Journal of Fluid Mechanics, **936**, p. A2.

[16] Bao, D., Borée, J., Sicot, C., and Roebroeck, C., 2024, "Influence of vehicle back shape on wheel-vehicle aerodynamic interactions: a model study," Experiments in Fluids, **65**(4), p. 50.

[17] Pavia, G., Passmore, M. A., Varney, M., and Hodgson, G., 2020, "Salient three-dimensional features of the turbulent wake of a simplified square-back vehicle," Journal of Fluid Mechanics, **888**, p. A33.

[18] Bello-Millán, F., Mäkelä, T., Parras, L., del Pino, C., and Ferrera, C., 2016, "Experimental study on Ahmed's body drag coefficient for different yaw angles," Journal of Wind Engineering and Industrial Aerodynamics, **157**, pp. 140–144.

[19] Urquhart, M., Varney, M., Sebben, S., and Passmore, M., 2021, "Drag reduction mechanisms on a generic square-back vehicle using an optimised yaw-insensitive base cavity," Experiments in Fluids, **62**, p. 241.

[20] Strachan, R. K., Knowles, K., and Lawson, N. J., 2007, "The vortex structure behind an Ahmed reference model in the presence of a moving ground plane," Experiments in Fluids, **42**, pp. 659–669.

[21] Rejniak, A. A. and Gatto, A., 2021, "Influence of Rotating Wheels and Moving Ground Use on the Unsteady Wake of a Small-Scale Road Vehicle," Flow, Turbulence and Combustion, **106**, pp. 109–137.

[22] Anderson, J., 2017, *Fundamentals of Aerodynamics*, McGraw-Hill series in aeronautical and aerospace engineering, McGraw-Hill Education.

[23] Markina, A. A., Lukashuk, A. D., Chepkasov, S. N., and Starovoytenko, A. V., 2020, "Improving aerodynamic characteristics for drag reduction of heavy truck," IOP Conference Series: Materials Science and Engineering, **862**(3), p. 032032.

[24] Beaudoin, J.-F. and Aider, J.-L., 2008, "Drag and lift reduction of a 3D bluff body using flaps," Experiments in fluids, **44**(4), pp. 491–501.

[25] Fourrié, G., Keirsbulck, L., Labraga, L., and Gilliéron, P., 2011, "Bluff-body drag reduction using a deflector," Experiments in Fluids, **50**, pp. 385–395.

[26] Aider, J.-L., Beaudoin, J.-F., and Wesfreid, J. E., 2010, "Drag and lift reduction of a 3D bluff-body using active vortex generators," Experiments in Fluids, **48**, pp. 771–789.

[27] Giannenas, A. E., Laizet, S., and Rigas, G., 2022, "Harmonic forcing of a laminar bluff body wake with rear pitching flaps," Journal of Fluid Mechanics, **945**, p. A5.

[28] Garcia de la Cruz, J., Brackston, R., and Morrison, J., 2017, "Adaptive Base-Flaps Under Variable Cross-Wind," SAE Technical Paper, pp. 2017–01–7000,.

[29] Camacho-Sánchez, J. M., Lorite-Díez, M., Jiménez-González, J. I., Cadot, O., and Martínez-Bazán, C., 2023, "Experimental study on the effect of adaptive flaps on the aerodynamics of an Ahmed body," Phys. Rev. Fluids, **8**, p. 044605.

[30] Muñoz-Hervás, J., Lorite-Díez, M., García-Baena, C., and Jiménez-González, J., 2024, "Experimental investigation of rear flexible flaps interacting with the wake dynamics behind a squareback Ahmed body," Journal of Fluids and Structures, **127**, p. 104124.

[31] Haffner, Y., Castelain, T., Borée, J., and Spohn, A., 2021, "Manipulation of three-dimensional asymmetries of a turbulent wake for drag reduction," Journal of Fluid Mechanics, **912**, p. A6.

[32] Li, R., Borée, J., Noack, B. R., Cordier, L., and Harambat, F., 2019, "Drag reduction mechanisms of a car model at moderate yaw by bi-frequency forcing," Physical Review Fluids, **4**, p. 034604.

[33] Kim, J. and Choi, H., 2005, "Distributed forcing of flow over a circular cylinder," Physics of Fluids, **17**(3), p. 033103.

[34] Corke, T. C., Post, M. L., and Orlov, D. M., 2009, "Single dielectric barrier discharge plasma enhanced aerodynamics: physics, modeling and applications," Experiments in Fluids, **46**, p. 1.

[35] Benard, N., Cattafesta, I., L. N., Moreau, E., Griffin, J., and Bonnet, J. P., 2011, "On the benefits of hysteresis effects for closed-loop separation control using plasma actuation," Physics of Fluids, **23**(8), p. 083601.

[36] Benard, N. and Moreau, E., 2014, "Electrical and mechanical characteristics of surface AC dielectric barrier discharge plasma actuators applied to air flow control," Experiments in Fluids, **55**, p. 1846.

[37] Corke, T. C., Enloe, C. L., and Wilkinson, S. P., 2010, "Dielectric Barrier Discharge Plasma Actuators for Flow Control," Annual Review of Fluid Mechanics, **42**, pp. 505–529.

[38] Kaneko, Y., Yamanaka, A., and Nishida, H., 2024, "Data assimilation to determine the electrohydrodynamic force of plasma actuator," Sensors and Actuators A: Physical, **372**, p. 115320.

[39] Sato, S., Enokido, T., Ashikawa, K., Matsubara, M., Kanie, K., and Ohnishi, N., 2021, "Development of a flexible dielectric-barrier-discharge plasma actuator fabricated by inkjet printing using silver nanoparticles-based ink," Sensors and Actuators A: Physical, **330**, p. 112823.

[40] Asada, K., Ninomiya, Y., Fujii, K., and Oyama, A., 2009, "Airfoil Flow Experiment on the Duty Cycle of DBD Plasma Actuator," *47th AIAA Aerospace Sciences Meeting including The New Horizons Forum and Aerospace Exposition*, doi: 10.2514/6.2009-531.

[41] Shimomura, S., Sekimoto, S., Oyama, A., Fujii, K., and Nishida, H., 2020, "Closed-Loop Flow Separation Control Using the Deep Q Network over Airfoil," AIAA Journal, **58**(10), pp. 4260–4270.

[42] Zhang, X., Choi, K.-S., Huang, Y., and Li, H.-x., 2019, "Flow control over a circular cylinder using virtual moving surface boundary layer control," Experiments in fluids, **60**, p. 104.

[43] Wang, L., Alam, M. M., and Zhou, Y., 2021, "Drag reduction of circular cylinder using linear and sawtooth plasma actuators," Physics of Fluids, **33**(12), p. 124105.

[44] Rodrigues, F., Abdollahzadehsangroudi, M., Nunes-Pereira, J., and Páscoa, J., 2022, "Recent developments on dielectric barrier discharge (DBD) plasma actuators for icing mitigation," Actuators, **12**(1), p. 5.

[45] Boeuf, J. P., Lagmich, Y., Unfer, T., Callegari, T., and Pitchford, L. C., 2007, "Electrohydrodynamic force in dielectric barrier discharge plasma actuators," Journal of Physics D: Applied Physics, **40**(3), p. 652.

[46] Moreau, E., Cazour, J., and Benard, N., 2018, "Influence of the air-exposed active electrode shape on the electrical, optical and mechanical characteristics of a surface dielectric barrier discharge plasma actuator," Journal of Electrostatics, **93**, pp. 146–153.

[47] Nakano, A. and Nishida, H., 2019, "The effect of the voltage waveform on performance of dielectric barrier discharge plasma actuator," Journal of Applied Physics, **126**(17), p. 173303.

[48] Hehner, M. T., Gatti, D., and Kriegseis, J., 2019, "Stokes-layer formation under absence of moving parts—A novel oscillatory plasma actuator design for turbulent drag reduction," Physics of Fluids, **31**(5), p. 051701.

[49] Da Silva, G. P. G., Eguea, J. P., Croce, J. A. G., and Catalano, F. M., 2020, "Slat aerodynamic noise reduction using dielectric barrier discharge plasma actuators," Aerospace Science and Technology, **97**, p. 105642.

[50] Rodrigues, F., Pascoa, J., and Trancossi, M., 2018, "Heat generation mechanisms of DBD plasma actuators," Experimental thermal and fluid science, **90**, pp. 55–65.

[51] Abdollahzadeh, M., Páscoa, J. C., and Oliveira, P. J., 2014, "Two-dimensional numerical modeling of interaction of micro-shock wave generated by nanosecond plasma actuators and transonic flow," Journal of Computational and Applied Mathematics, **270**, pp. 401–416.

[52] Kaneko, Y., Nishida, H., and Tagawa, Y., 2022, "Visualization of the Electrohydrodynamic and Thermal Effects of AC-DBD Plasma Actuators of Plate- and Wire-Exposed Electrodes," Actuators, **11**(2), p. 38.

[53] Meng, X., Hu, H., Li, C., Abbasi, A. A., Cai, J., and Hu, H., 2019, "Mechanism study of coupled aerodynamic and thermal effects using plasma actuation for anti-icing," Physics of Fluids, **31**(3), p. 037103.

[54] Zheng, J., Cui, Y., Zhao, Z., Li, J., and Khoo, B., 2016, "Investigation of airfoil leading edge separation control with nanosecond plasma actuator," Physical Review Fluids, **1**(7), p. 073501.

[55] Kim, D., Do, H., and Choi, H., 2020, "Drag reduction on a three-dimensional model vehicle using a wire-to-plate DBD plasma actuator," Experiments in Fluids, **61**, p. 135.

[56] Rodrigues, F. F., Moreira, M., and Pascoa, J., 2021, "Analysis and Implementation of Dielectric Barrier Discharge Plasma Actuators for Ground Vehicles Wake Reduction," p. V003T05A014, doi: 10.1115/FEDSM2021-65735.

[57] Vernet, J. A., Örlü, R., Söderblom, D., Elofsson, P., and Alfredsson, P. H., 2018, "Plasma streamwise vortex generators for flow separation control on trucks: A proof-of-concept experiment," Flow, turbulence and combustion, **100**, pp. 1101–1109.

[58] Roy, S., Zhao, P., DasGupta, A., and Soni, J., 2016, "Dielectric barrier discharge actuator for vehicle drag reduction at highway speeds," AIP Advances, **6**(2), p. 025322.

[59] El-Alti, M., Chernoray, V., Kjellgren, P., Hjelm, L., and Davidson, L., 2016, "Computations and Full-Scale Tests of Active Flow Control Applied on a VOLVO Truck-Trailer," *The Aerodynamics of Heavy Vehicles III*, A. Dillmann and A. Orellano, eds., Springer International Publishing, Cham, pp. 253–267.

[60] Westerweel, J. and Scarano, F., 2005, "Universal outlier detection for PIV data," Experiments in fluids, **39**, pp. 1096–1100.

[61] Ahmed, S. R., 1983, "Influence of Base Slant on the Wake Structure and Drag of Road Vehicles," Journal of Fluids Engineering, **105**(4), pp. 429–434.

[62] Sekimoto, S., Nonomura, T., and Fujii, K., 2017, "Burst-Mode Frequency Effects of Dielectric Barrier Discharge Plasma Actuator for Separation Control," AIAA Journal, **55**(4), pp. 1385–1392.

[63] Sato, M., Okada, K., Asada, K., Aono, H., Nonomura, T., and Fujii, K., 2020, "Unified mechanisms for separation control around airfoil using plasma actuator with burst actuation over Reynolds number range of 103–106," Physics of Fluids, **32**(2), p. 025102.

[64] Mishra, B. K. and Panigrahi, P. K., 2017, "Formation and characterization of the vortices generated by a DBD plasma actuator in burst mode," Physics of Fluids, **29**(2), p. 024104.

[65] Emori, K., Kaneko, Y., and Nishida, H., 2022, "Classification of flow-field patterns in burst-mode actuation of a dielectric-barrier-discharge plasma actuator," Physics of Fluids, **34**(2), p. 023601.

Journal of Fluids Engineering. February 19, 2025;
Accepted manuscript posted May 23, 2025. 10.1115/1.4068762

Table Caption List

Table 1 Experimental conditions on rear flap length, angle, and mounting surface

Figure Caption List

Fig. 1 Power flow diagram of plasma actuator.

Fig. 2 Bluff body model used in the experiments. The fairing (black) is mounted to prevent the flow separation at the front of the model and maintain the attached flow just before the rear flaps. (a) Picture and (b) configuration of the model. The height H, width W, and length L of the model is respectively defined as 0.250, 0.190, and 0.732 m.

Fig. 3 (a) Schematic drawing of a flap with deflection angle α. (b) Plasma actuators are made with the acrylic plate as dielectric. Copper tapes are attached on both sides of the acrylic plate asymmetrically with 0 mm overlap.

Fig. 4 Two types of flaps. (a) Top flap and (b) Side flaps. In both cases, the additional flat acrylic plates are mounted on the surfaces where the PA-installed flaps are not mounted.

Fig. 5 Wind tunnel and measurement system of aerodynamic drag.

Fig. 6 Sampling duration convergence of force measurement. The plotted data are obtained under the condition of $l^* = 0.04$, $\alpha = 10°$, with the PA actuation.

Fig. 7 PIV measurements for two cross-sections are conducted depending on the flap type. (a) Visualization of the flowfield along the $x - z$ cross-section perpendicular to the top flap and wind tunnel floor. (b) Visualization of flowfield along a $x - y$ cross section parallel to the wind tunnel floor at the height of 208 mm (i.e., $z/H = 0.83$)

Fig. 8 Results of drag measurements on a top-flap mounted truck model. (a) Drag C_D and (b) Drag reduction rate DR as a function of flap deflection angle α. The diamond and square markers show the results of long ($l^* = 0.20$) and short ($l^* = 0.04$) flap, respectively. C_D reduction can be achieved when PA is actuated with a short flap.

Fig. 9 Velocity fields when the long flap is mounted on top of the model. (a) $\alpha = 0°$ without PA actuation (baseline), (b) $\alpha = 15°$ without PA actuation, (c) $\alpha = 25°$ without PA actuation, and (d) $\alpha = 25°$ with PA actuation. The dashed lines in (b), (c), and (d) represent the 15° lines. Although flow is deflected, and the wake region is modified at (d) $\alpha = 25°$ with PA actuation compared with (b), C_D of $\alpha = 25°$ with PA actuation is larger than that of $\alpha = 15°$ without PA actuation. The reason why the drag is not decreased nevertheless the flow is drastically modified is considered to be the pressure on the flap becomes drag.

Fig. 10 Flowfields when the short flap is mounted on top of the model. (a) $\alpha = 0°$ without PA actuation (baseline), (b) $\alpha = 20°$ without PA actuation, and (c) $\alpha = 20°$ with PA actuation. The dashed lines in (b), (c) represent the 20° lines. Although the PA actuation above the short flap at $\alpha = 20°$ shows slight effect on wake, drag can be reduced.

Fig. 11 Results of drag measurements on side-flaps mounted model. (a) Drag C_D and (b) drag reduction rate DR as a function of side flap angles α. The circle and triangle markers show the results of long and short flaps, respectively. As the top flap, C_D reduction can be achieved when PA is actuated on short flap as well as the PA is mounted on top flap.

Fig. 12 Flowfields of long-side-flaps mounted model. (a) $\alpha = 0°$ without PA actuation (baseline) and (b) $\alpha = 15°$. The upper and bottom of (b) respectively show the flowfield without and with PA actuation. Dashed white lines in (b) represent the 15° lines along the flap. The long flaps mounted on the side of the model can deflect side flows drastically and achieve a considerable decrease in C_D. However, PA actuation in this condition has little effect, and there is no change in C_D.

Fig. 13 Flowfields of short-side-flap mounted model. (a) $\alpha = 0°$ without PA actuation (baseline), (b) $\alpha = 15°$, and (c) $\alpha = 30°$. The upper and bottom of (b) and (c) respectively show the flowfield without and with PA actuation. Dashed white lines correspond to the 15° lines along the flap. In both $\alpha = 15°$ and 30°, PA actuation above short flaps can get the wake region narrower and decrease in C_D. This flow control effect does not do as well as that of long flaps (Fig. 12).

437 **Tables**

Table 1 Experimental conditions on rear flap length, angle, and mounting surface

Mounting surface	Flap length $l^* = l/H$ [-]	Flap angle α [°]
Top	0.20	0, 10, 15, 20, 25, 30
Top	0.04	0, 10, 15, 20, 25, 30
Side	0.20	0, 10, 15, 20, 25, 30
Side	0.04	0, 10, 15, 20, 25, 30

Journal of Fluids Engineering. February 19, 2025;
Accepted manuscript posted May 23, 2025. 10.1115/1.4068762

Figures

438

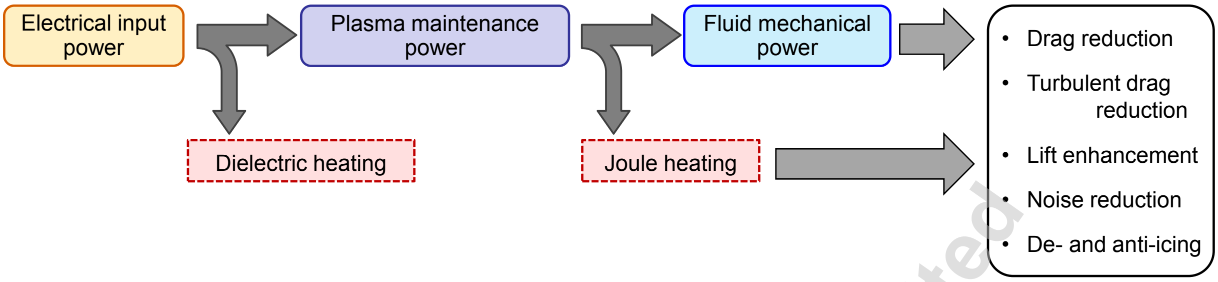

Fig. 1 Power flow diagram of plasma actuator.

Journal of Fluids Engineering. February 19, 2025;
Accepted manuscript posted May 23, 2025. 10.1115/1.4068762

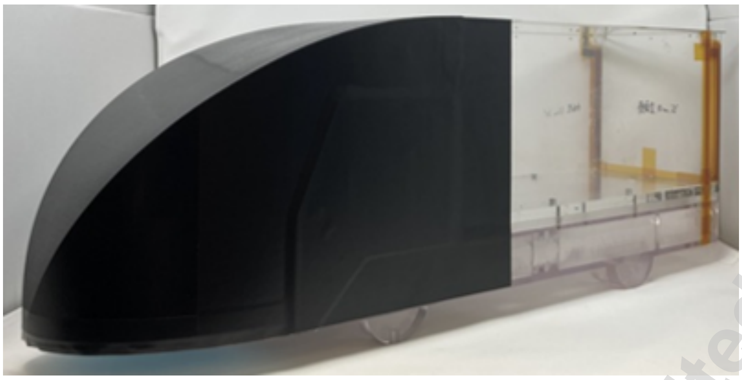

(*a*)

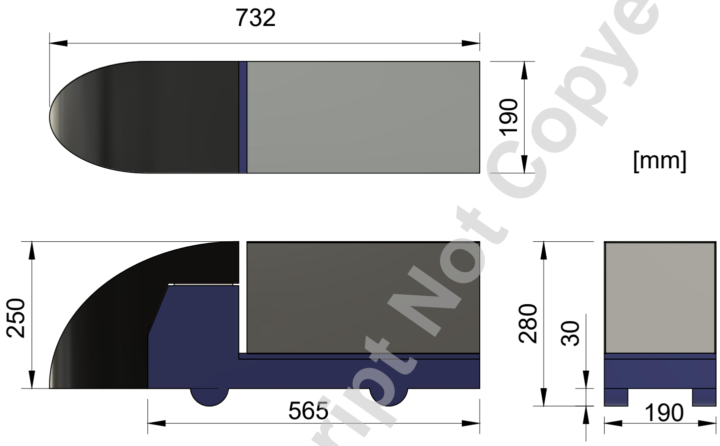

(*b*)

Fig. 2 Bluff body model used in the experiments. The fairing (black) is mounted to prevent the flow separation at the front of the model and maintain the attached flow just before the rear flaps. (*a*) Picture and (*b*) configuration of the model. The height *H*, width *W*, and length *L* of the model is respectively defined as 0.250, 0.190, and 0.732 m.

Journal of Fluids Engineering. February 19, 2025;
Accepted manuscript posted May 23, 2025. 10.1115/1.4068762

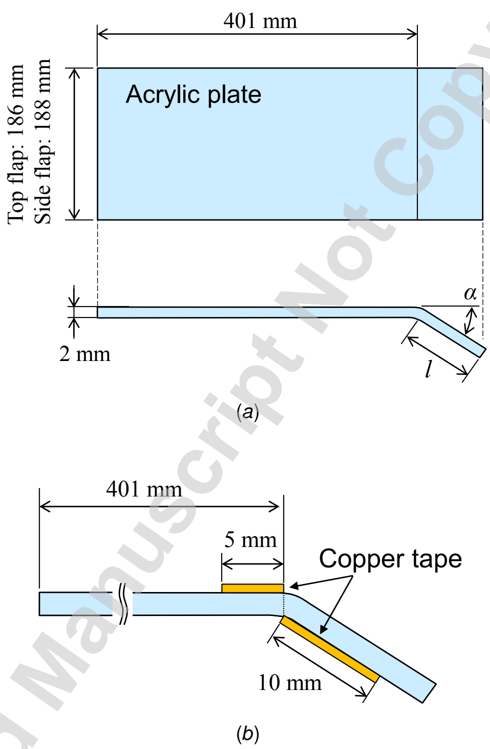

Fig. 3 (*a*) Schematic drawing of a flap with deflection angle α. (*b*) Plasma actuators are made with the acrylic plate as dielectric. Copper tapes are attached on both sides of the acrylic plate asymmetrically with 0 mm overlap.

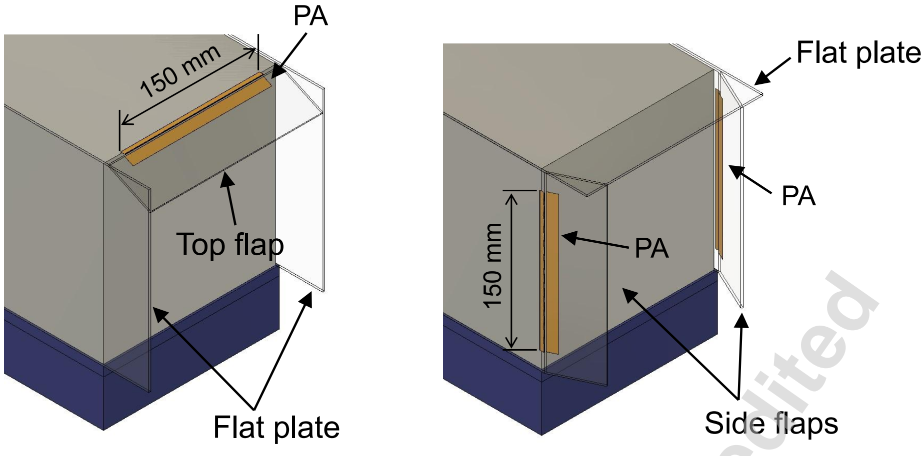

Fig. 4 Two types of flaps. (*a*) Top flap and (*b*) Side flaps. In both cases, the additional flat acrylic plates are mounted on the surfaces where the PA-installed flaps are not mounted.

Journal of Fluids Engineering. February 19, 2025;
Accepted manuscript posted May 23, 2025. 10.1115/1.4068762

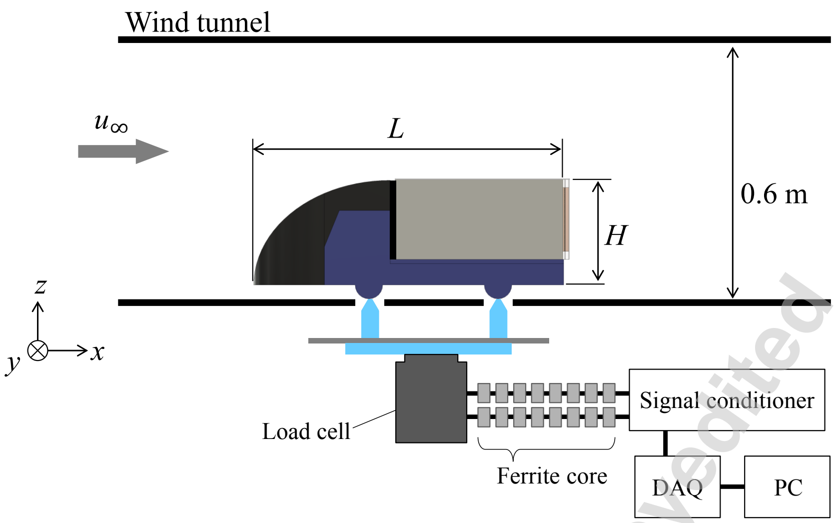

Fig. 5 Wind tunnel and measurement system of aerodynamic drag.

Journal of Fluids Engineering. February 19, 2025;
Accepted manuscript posted May 23, 2025. 10.1115/1.4068762

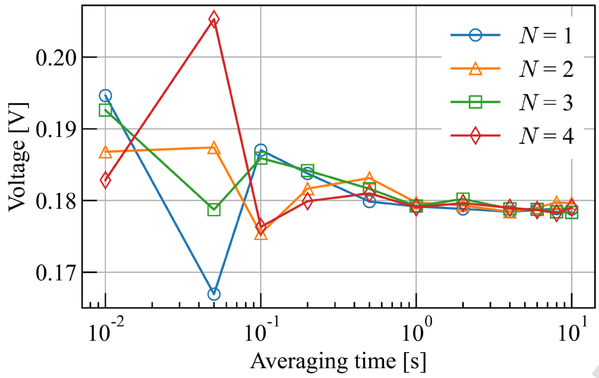

Fig. 6 Sampling duration convergence of force measurement. The plotted data are obtained under the condition of l^* = 0.04, α = 10°, with the PA actuation.

Journal of Fluids Engineering. February 19, 2025;
Accepted manuscript posted May 23, 2025. 10.1115/1.4068762

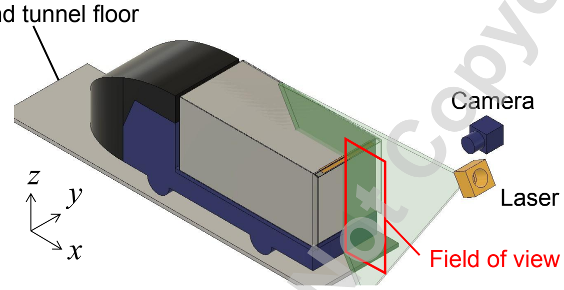

(a)

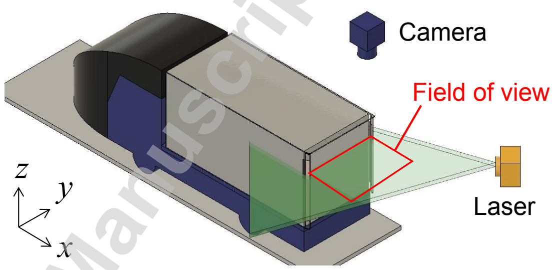

(b)

Fig. 7 PIV measurements for two cross-sections are conducted depending on the flap type. (a) Visualization of the flowfield along the $x-z$ cross-section perpendicular to the top flap and wind tunnel floor. (b) Visualization of flowfield along a $x-y$ cross section parallel to the wind tunnel floor at the height of 208 mm (i.e., $z/H = 0.83$).

Journal of Fluids Engineering. February 19, 2025;
Accepted manuscript posted May 23, 2025. 10.1115/1.4068762

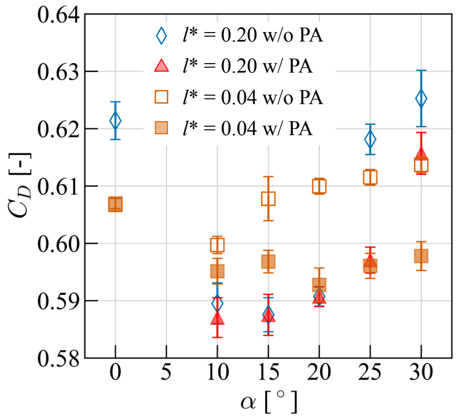

(a)

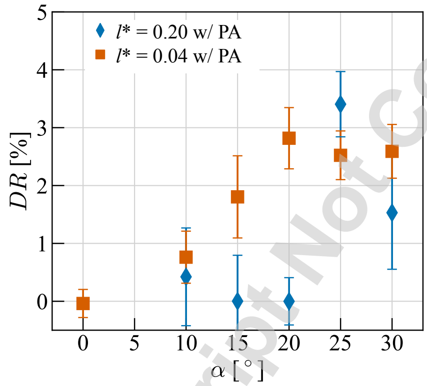

(b)

Fig. 8 Results of drag measurements on a top-flap mounted truck model. (a) Drag C_D and (b) Drag reduction rate DR as a function of flap deflection angle α. The diamond and square markers show the results of long ($l^* = 0.20$) and short ($l^* = 0.04$) flap, respectively. C_D reduction can be achieved when PA is actuated with a short flap.

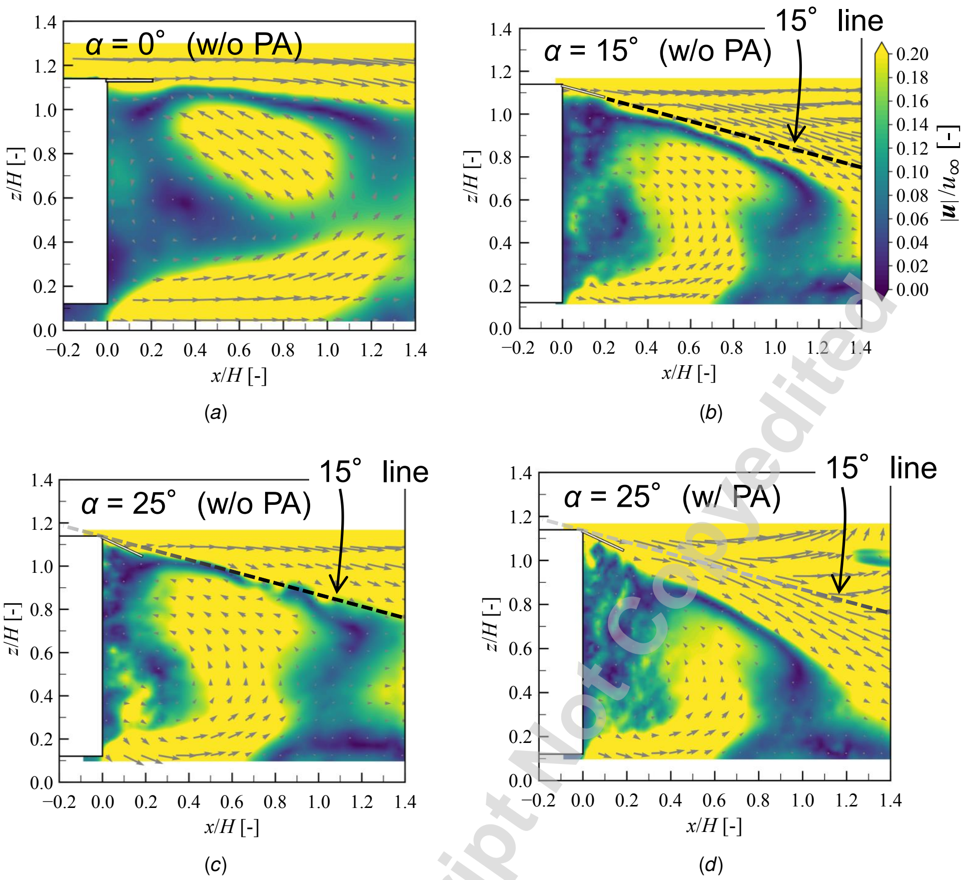

Fig. 9 Velocity fields when the long flap is mounted on top of the model. (a) α = 0° without PA actuation (baseline), (b) α = 15° without PA actuation, (c) α = 25° without PA actuation, and (d) α = 25° with PA actuation. The dashed lines in (b), (c), and (d) represent the 15° lines. Although flow is deflected, and the wake region is modified at (d) α = 25° with PA actuation compared with (b), C_D of α = 25° with PA actuation is larger than that of α = 15° without PA actuation. The reason why the drag is not decreased nevertheless the flow is drastically modified is considered to be the pressure on the flap becomes drag.

Journal of Fluids Engineering. February 19, 2025;
Accepted manuscript posted May 23, 2025. 10.1115/1.4068762

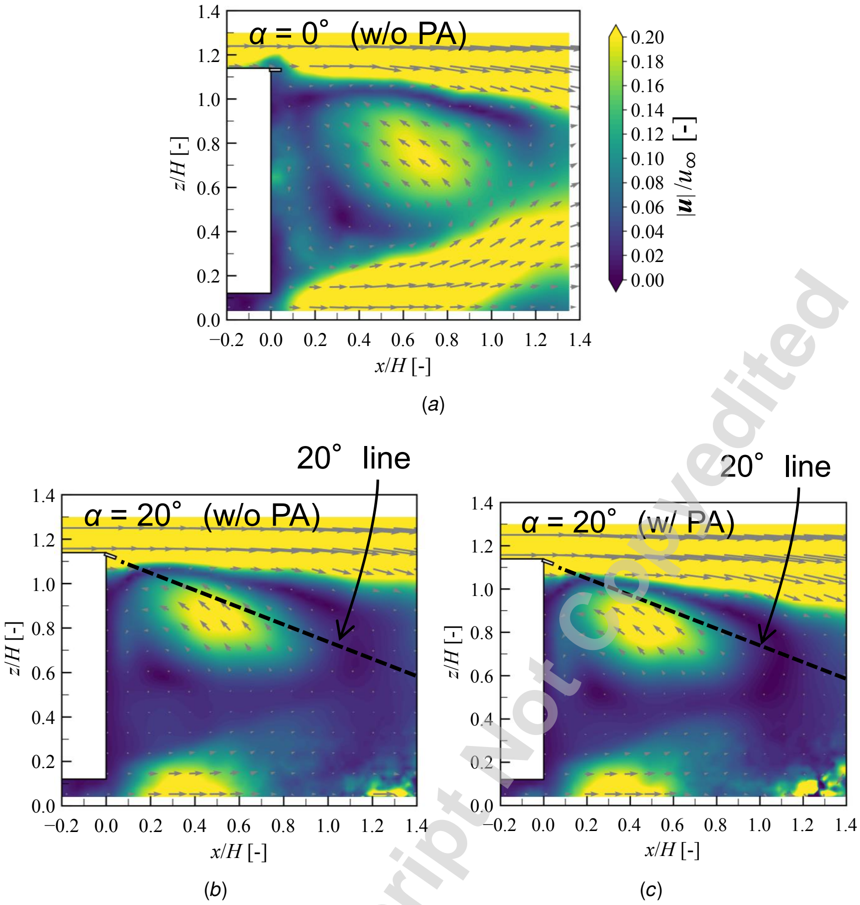

Fig. 10 **Flowfields when the short flap is mounted on top of the model. (a) α = 0° without PA actuation (baseline), (b) α = 20° without PA actuation, and (c) α = 20° with PA actuation. The dashed lines in (b), (c) represent the 20° lines. Although the PA actuation above the short flap at α = 20° shows slight effect on wake, drag can be reduced.**

Journal of Fluids Engineering. February 19, 2025;
Accepted manuscript posted May 23, 2025. 10.1115/1.4068762

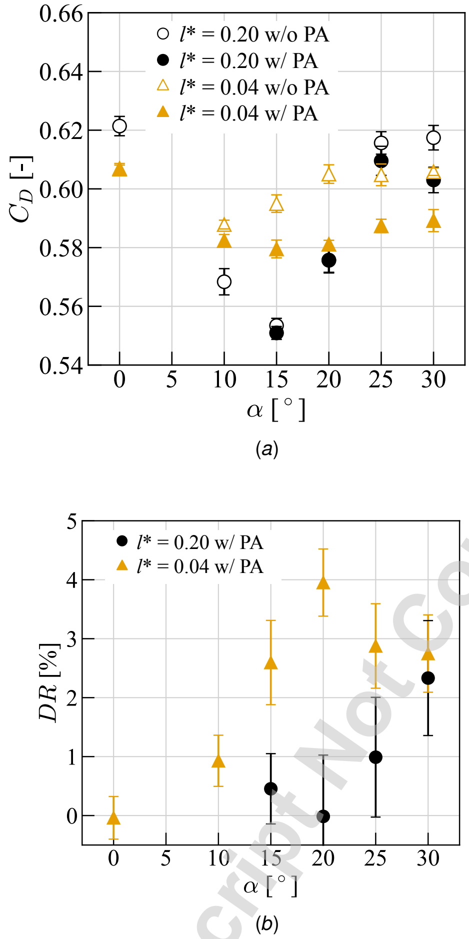

Fig. 11 Results of drag measurements on side-flaps mounted model. (a) Drag C_D and (b) drag reduction rate DR as a function of side flap angles α. The circle and triangle markers show the results of long and short flaps, respectively. As the top flap, C_D reduction can be achieved when PA is actuated on short flap as well as the PA is mounted on top flap.

Journal of Fluids Engineering. February 19, 2025;
Accepted manuscript posted May 23, 2025. 10.1115/1.4068762

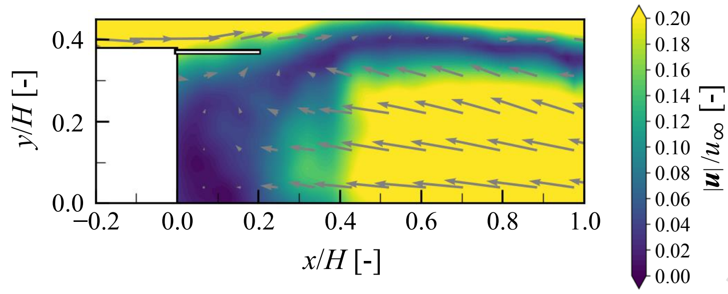

(a)

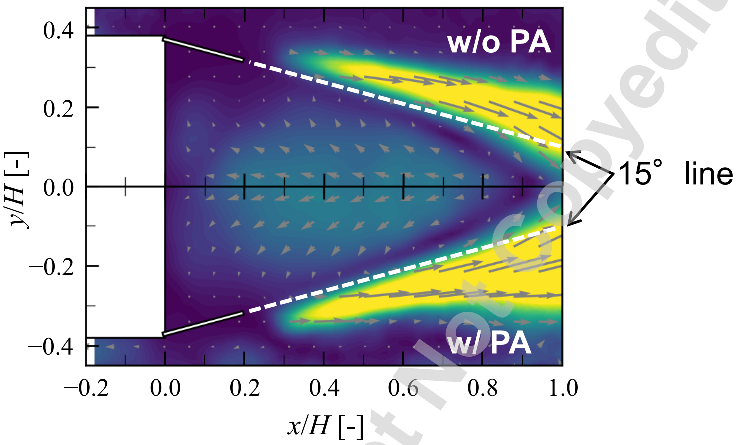

(b)

Fig. 12 Flowfields of long-side-flaps mounted model. (a) α = 0° without PA actuation (baseline) and (b) α = 15°. The upper and bottom of (b) respectively show the flowfield without and with PA actuation. Dashed white lines in (b) represent the 15° lines along the flap. The long flaps mounted on the side of the model can deflect side flows drastically and achieve a considerable decrease in C_D. However, PA actuation in this condition has little effect, and there is no change in C_D.

Journal of Fluids Engineering. February 19, 2025;
Accepted manuscript posted May 23, 2025. 10.1115/1.4068762

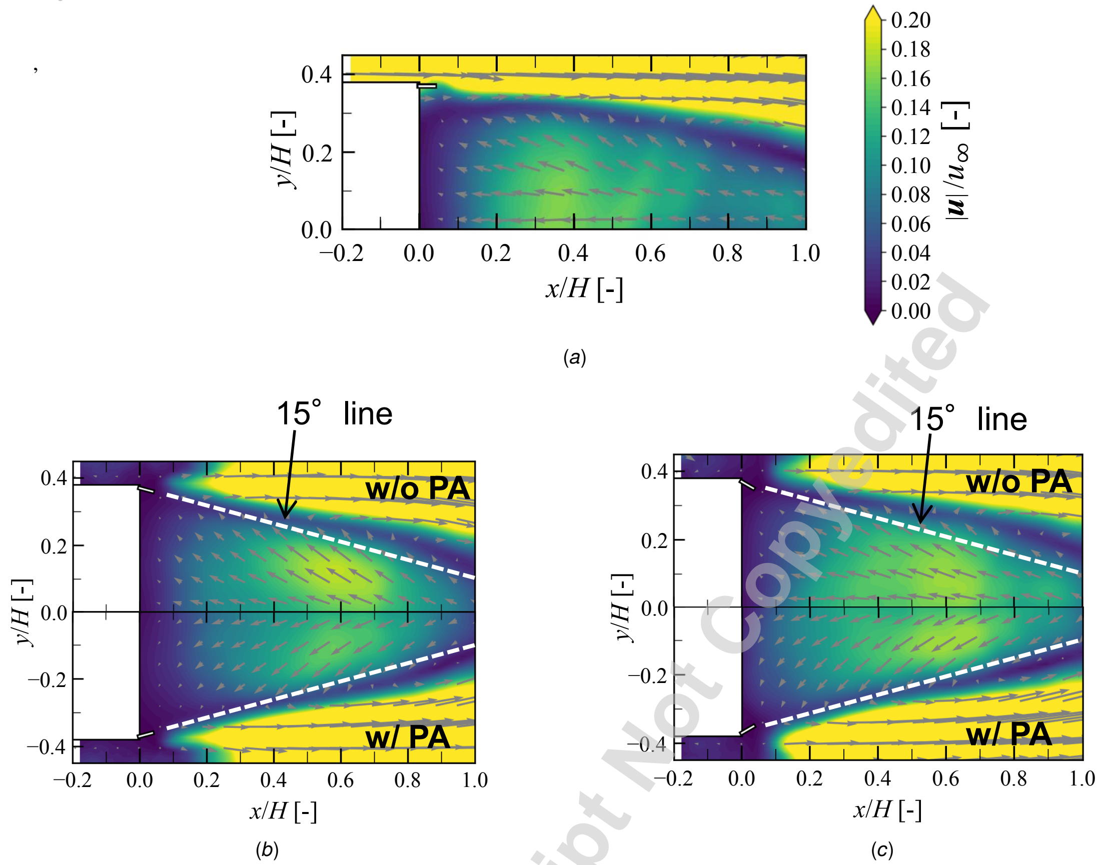

Fig. 13 **Flowfields of short-side-flap mounted model. (a) α = 0° without PA actuation (baseline), (b) α = 15°, and (c) α = 30°. The upper and bottom of (b) and (c) respectively show the flowfield without and with PA actuation. Dashed white lines correspond to the 15° lines along the flap. In both α = 15° and 30°, PA actuation above short flaps can get the wake region narrower and decrease in C_D. This flow control effect does not do as well as that of long flaps (Fig. 12).**